Research Paper

A novel multi-scale µCT characterization method to quantify biogenic carbonate production

V. Chandra [a,e,*], R. Sicat [b], F. Benzoni [c], V. Vahrenkamp [a], V. Bracchi [d]

[a] *Physical Sciences and Engineering, King Abdullah University of Science and Technology, Thuwal, Saudi Arabia*
[b] *Visualization Core Lab, King Abdullah University of Science and Technology, Thuwal, Saudi Arabia*
[c] *Biological and Environmental Science and Engineering, King Abdullah University of Science and Technology, Thuwal, Saudi Arabia*
[d] *Department of Earth and Environmental Sciences, University of Milano-Bicocca, Milan, Italy*
[e] *Saudi Aramco, Dhahran, Saudi Arabia*

ARTICLE INFO

ABSTRACT

Biogenic carbonate structures such as rhodoliths and foraminiferal-algal nodules are a significant part of marine carbonate production and are being increasingly used as paleoenvironmental indicators for predictive modeling of the global carbon cycle and ocean acidification research. However, traditional methods to characterize and quantify the carbonate production of biogenic nodules are typically limited to two-dimensional analysis using optical and electron microscopy. While micro-computed tomography (µCT) is an excellent tool for 3D analysis of inner structures of geomaterials, the trade-off between sample size and image resolution is often a limiting factor. In this study, we address these challenges by using a novel multi-scale µCT image analysis methodology combined with electron microscopy, to visualize and quantify the carbonate volumes in a biogenic calcareous nodule. We applied our methodology to a foraminiferal-algal nodule collected from the Red Sea along the coast of NEOM, Saudi Arabia. Integrated µCT and SEM image analyses revealed the main biogenic carbonate components of this nodule to be encrusting foraminifera (EF) and crustose coralline algae (CCA). We developed a multi-scale µCT analysis approach for this study, involving a hybrid thresholding and machine-learning based image segmentation. We utilized a high resolution µCT scan from the sample as a ground-truth to improve the segmentation of the lower resolution full volume µCT scan which provided reliable volumetric quantification of the EF and CCA layers. Together, the EF and CCA layers contribute to approximately 65.5 % of the studied FAN volume, corresponding to 69.01 cm^3 and 73.32 cm^3 respectively, and the rest is comprised of sediment infill, voids and other minor components. Moreover, volumetric quantification results in conjunction with CT density values, indicate that the CCA layers are associated with the highest amount of carbonate production within this foraminiferal-algal nodule. The methodology developed for this study is suitable for analyzing biogenic carbonate structures for a wide array of applications including quantification of carbonate production and studying the impact of ocean acidification on skeletal structures of marine calcifying organisms. In particular, the hybrid µCT image analysis we adopted in this study proved to be advantageous for the analysis of biogenic structures in which the textures and components of the internal layers are distinctly visible despite having an overlap in the range of CT density values.

1. Introduction

Biological carbonate production in the oceans is an important contributor to the global marine carbonate factory and biogeochemical cycles (Schrag et al., 2013; Gilbert et al., 2022). Marine calcifiers such as corals, mollusks, foraminifera, bryozoans, or red-/green algae precipitate calcium carbonate, usually in the form of high magnesium calcite (HMC) or aragonite. These organisms can be particularly productive, as they form stable structures at the seafloor like reefs or, upon death, break down by physical, chemical, and biological erosion processes and accumulate on the seafloor (Perry and Smithers, 2011). For example, neritic carbonate production has been estimated to be approximately 2.5 Gt year^{-1}

---

* Corresponding author.
  E-mail address: viswasanthi.chandra@gmail.com (V. Chandra).

(Milliman and Droxler, 1995; Heap et al., 2009). The most well-known contributors to shallow marine carbonate production are coral reefs that form complex structures covering a total area of more than 250,000 km^2 (Spalding and Grenfell, 1997; Vecsei, 2004). However, there is growing evidence that organisms such as Crustose Coralline Algae (CCA) that form smaller reefal structures or nodular macroid (e.g., rhodoliths) beds also contribute significantly to biogenic carbonate production (Cornwall et al., 2023; Bracchi et al., 2023).

Macroids (=oncoids larger than 1 cm, Peryt, 1983) are biogenic carbonate nodules made by encrusting metazoans or protozoans, sometimes associated with calcareous algae (Peryt, 1983). They form more or less concentric structures with an irregular layering pattern, related to the development of one or more carbonate-producing organisms such as corals (coralliths), bryozoans (bryoliths), crustose coralline algae (rhodoliths), and foraminiferal-algal association (foraminiferal-algal nodules) (Gill and Coates, 1977; Bosence, 1983; Dade, 1984; Reid and Macintyre, 1988; Prager and Ginsburg, 1989). These nodules preserve sensitive records of their depositional environment's evolution as a function of shape and growth-form of skeletal components, biotic composition and diagenetic history, and are therefore considered useful as paleoenvironmental indicators (Logan et al., 1969; Bosellini and Ginsburg, 1971; Toomey, 1975; Orzag-Sperber et al., 1977; Focke and Gebelein, 1978; Minoura and Nakamori, 1982; Bosence and Pedley, 1982; Bosence, 1983; Scoffin et al., 1985; Reid and Macintyre, 1988). Moreover, nodules can colonize the seafloor, for example rhodoliths from the intertidal zone down to 150 m deep (Bosence, 1983; Foster, 2001; Vale et al., 2018) or foraminiferal-algal nodules from the mesophotic (Bassi et al., 2012; Bracchi et al., 2023), aggregating into extensive habitat (the so-called beds), which often represent a key-component of the seascape. Furthermore, being composed of carbonates, nodules are part of the carbonate factory (Schlager, 2000), and are relevant for the carbonate-budget calculation. Therefore, they should be taken into account for the predictive modeling of the global carbon cycle (Ridgwell and Zeebe, 2005). However, there is a severe lack of existing data on the contribution of biogenic nodules to the biogenic carbonate budget. For example, recent empirical estimations suggest that the marine carbonate deposits formed by coralline algae represent a total potential carbon sink of 4×108 t C/yr (van der Heijden and Kamenos, 2015), indicating that rhodolith beds may represent a significant yet underappreciated carbon store (Hill et al., 2015; Macreadie et al., 2017). More recently, Bracchi et al. (2023) studied the foraminiferal-algal nodule habitat in the Red Sea and concluded that their contribution to the mesophotic carbonate budget is up to 66 g m^{-2} year^{-1} and account for at least 980 megatons of calcium carbonate over an area of 95 km^2 between 58.6 and 131.8 m of water depth, underscoring their ecological significance. Bosence and Wilson (2003) detail a number of methods for estimating carbonate production. Dry-weighting is a simple and commonly used to estimate carbonate production, but this method only results in a gross production value. Moreover, dry-weight approach does not allow the study of the nodule in the natural setting, since the drying process will also kill the organisms on the nodule. Furthermore, the technical and economic efforts for exploring and sampling this kind of nodule-dominated habitats are typically high, especially in the deeper subsea environments that are challenging to access. Therefore, the development of suitable techniques and standardized methods for their characterization is essential.

Traditionally, the widely used methods for characterization of internal components of biogenic macroid in the laboratory are mainly based on destructive methods including the preparation of appropriate samples for their observation using optical and scanning electron microscopy. These methods rely heavily on specialized know-how and hands-on expertise for appropriate sample preparation and extraction of representative sub-samples for studying the internal features. Although it is necessary to subject a few representative samples to such destructive methods, it may not be desirable to apply these destructive methods to a large number of samples, in the interest of minimizing the disruption to natural habitats. Moreover, these methods are labor- and time-intensive, which hinder the study of statistically large enough number of samples.

The description of inner components is often based on manual segmentation of biotic components to obtain semi-quantitative results of the inner structure compositions in two-dimensions (Reid and Macintyre, 1988; Di Geronimo et al., 2002). However, recent advances in x-ray micro-Computed Tomography (μCT) have led to improved characterization methods to study biogenic samples. μCT imaging acquires precise three-dimensional images (tomograms) of objects non-destructively and has been extensively used for earth and environmental science studies (Cnudde and Boone, 2013). μCT imaging is therefore ideal for 3D reconstruction of cross-sectional geometry and quantification of biogenic carbonate structures. μCT allows the visualization of carbonate skeletons or the highly-mineralized structures of similar density, and voids/-cavities, even when they are occluded by sedimentary matrix (Nitsch et al. 2015; Bracchi et al., 2022). μCT has been widely used to study invertebrate fauna such as corals (e.g., Laforsch et al. 2008; Speijer et al., 2008; Naumann et al., 2009; Roche et al., 2010; Enochs et al., 2016a; Fordyce et al., 2020; Li et al., 2021), mollusks (Marcondes Machado et al., 2019; Martínez-Sanjuán et al., 2022), coralline algae (Bressan et al., 2007a, 2007b; Chan et al., 2017) and the effect of climate change on their biomineralization potential. Indeed, μCT imaging has been applied as a non-destructive method to analyze bio-erosional features in biogenic nodules, allowing a detailed understanding of complex endolithic structures and formation patterns in three-dimensions in various substrates (e.g., Schönberg and Shields, 2008; Tapanila, 2008; Bromley et al., 2008; Leal et al., 2012). This technique has also been used to improve the understanding of the fauna associated with living and fossil rhodoliths (Bressan et al., 2007a, 2007b; Leal et al., 2012; Teichert, 2014; Torrano-Silva et al. 2015). However, only a few studies have utilized μCT imaging to study macroids and other biogenic carbonate structures for quantitative analysis, for example, to compute volumes of inner components of biogenic carbonate structures. Such methodologies that can support non-destructive quantitative analysis can also optimize the manual efforts into subsampling and usage of the limited sample material.

The main challenges involved in quantitative μCT analysis of internal structures of biogenic carbonate samples include: i) Trade-off between sample size and resolution, ii) Thin-layers of biogenic material resulting in partial volume effect (several materials/classes are contained in a single pixel/voxel), iii) Removal of additional surficial growths or background materials, iv) Multiple materials with overlapping or similar grey-scale range, and v) Manual work involved in segmenting each scan. In this study, we aim to address these challenges by using a novel multi-scale μCT image analysis methodology combined with electron microscopy and a machine learning based image segmentation approach. To the best of our knowledge, this is the first study that employs Texture-Supervised Classification method to segment and quantify multiple inner components of macroids. We applied this methodology to one of the encrusting foraminiferal-algal nodules (hereby referred to as FANs) collected from the Red Sea, along the NEOM coast of the Red Sea (Saudi Arabia) during the NEOM-OceanX expedition Bracchi et al. (2023). The overarching aim of this study is to explore the potential of applying μCT imaging and machine learning based segmentation for providing a standardized method for the study of similar biogenic carbonate nodules and deposits.

2. Materials and methods

2.1. Foraminiferal-algal nodule (FAN) sample

The FAN sample NTN0035-17A used in this paper was collected within the framework of the scientific cruise, namely NEOM-OceanX "Deep Blue Expedition". The NEOM-OceanX expedition was conducted aboard the M/V OceanXplorer, between October and November 2020. The research cruise surveyed the NEOM area, along the Saudi Arabian coast, specifically from the Gulf of Aqaba (N 28,83085, E 34,823886) at a water depth of 102.8 m (Fig. 1). Triton 3300/3 submersibles named Neptune (NTN), equipped with a Schilling T4 hydraulic manipulator, was used for subsea research and sample collection.

2.2. μCT scanning

In order to perform 3D characterization of the internal structures of the FAN sample, we first performed x-ray μCT imaging (Supplementary Data Fig. S1). We used Tescan's CoreTOM^{TM} multi-scale x-ray system and Acquila^{TM} software to acquire the CT images used in this study. This system consists of a cone-beam setup (Hsieh, 2003) with an open type x-ray source and an x-ray detector with a large 2856 × 2856 pixels radiation-hard amorphous silicon flat panel. The maximum operational x-ray tube voltage and tube power are 180 kV and 300 W, respectively. The multi-scale x-ray set up allows the selection of 'volumes of interest' within the sample, which can be imaged at higher resolution than the full sample volume, for a given sample size and minimum possible source-sample distance. Two μCT scans were acquired, first a full-volume Low-Resolution CT scan (LRCT) with the optimal resolution of 70 μm of voxel size to accommodate the entire sample within the field of view. The second was a High-Resolution CT scan (HRCT) acquired for a sub-volume within the sample along the central axis. HRCT was acquired at 30 μm voxel size, which is the best resolution possible for the minimum source-sample distance and within the cone-beam configuration of CoreTOM^{TM}. The key x-ray CT parameters of these scans are summarized in Table 1. The x-ray projections were reconstructed into 3D tomographs using the Acquila^{TM} software using the filtered back projection method. Beam-hardening correction and ring-filter were applied to the data during the reconstruction step.

2.3. Optical and electron microscopy

After μCT scanning, the sample was impregnated with Epofix^{TM} resin to maintain the structural integrity, and then cut along its major axis. One half was used to produce thin sections to describe the layering structure and verify the observations made from the μCT images. Petrographic analysis of thin sections was performed using a Leica DM2700-P^{TM} optical microscope. The other half was used to prepare sub-samples for analysis under the Thermofisher-FEI Quattro^{TM} Scanning electronic Microscope (SEM) using the Everhart-Thornley Detector (ETD) and Energy Dispersive X-Ray (EDX) detectors, to characterize the microtextures and mineral composition of the main components of the nodule. Moreover, layer thickness and chamber/cell dimensions (height and diameter, $n = 30$) were measured using both thin section petrographs and SEM images.

2.4. Quantitative μCT image analysis

μCT image visualization and processing was performed using ThermoFisher Scientific Avizo^{TM} software. The μCT images of the low resolution full volume scan and the high resolution sub-volume scan were pre-processed before analysis by performing histogram equalization (Abdullah-Al-Wadud et al., 2007) and non-local means (NLM) filtering (Buades et al., 2005). The NLM filtering algorithm we used for denoising is based on an adaptive-manifolds approach, as described by Gastal and Oliveira (2012). Each target pixel was replaced with a weighted sum of pixels within a user-specified window around the target. The weights are based on the Gaussian kernel as a function of the similarity between the target pixel neighborhood and the pixel neighborhoods within the window. We used the interpretations based on the integrated visual analysis of μCT, TS petrography and SEM analysis to obtain the main classifications of labels to be extracted from the μCT images. As the first step to perform reliable quantitative analysis of the full FAN sample volume using LRCT, we segmented the sub-volume HRCT (30 μm voxel size) images. The goal was to obtain 'ground-truth' segmented volumes of the FAN sample using HRCT, which can then be used to improve the segmentation of the LRCT image and therefore improve the accuracy of the quantification of the various carbonate components in the full sample volume.

2.4.1. Segmentation of high resolution sub-volume μCT images

After the pre-processing steps, the HRCT image was cropped to remove the background voxels prior to performing segmentation. To segment the HRCT image we tested various combinations of routine thresholding methods and Texture Supervised Classification (TSC). Thresholding method typically involves assigning a specific greyscale range to each class to separate each component. We used the Ilastik pixel classifier (Berg et al., 2019) for TSC that implements a Random Forest classifier (Breiman, 2001) using mainly texture-based image features. TSC performs image segmentation based on local features, such as intensity, edges, and mainly texture, computed from the grey-value distributions of image pixels (Depeursinge et al., 2017). These textural features are fed into a Random Forest classifier (Breiman, 2001) that ultimately assigns a semantic class to each pixel in the target image. The TSC workflow
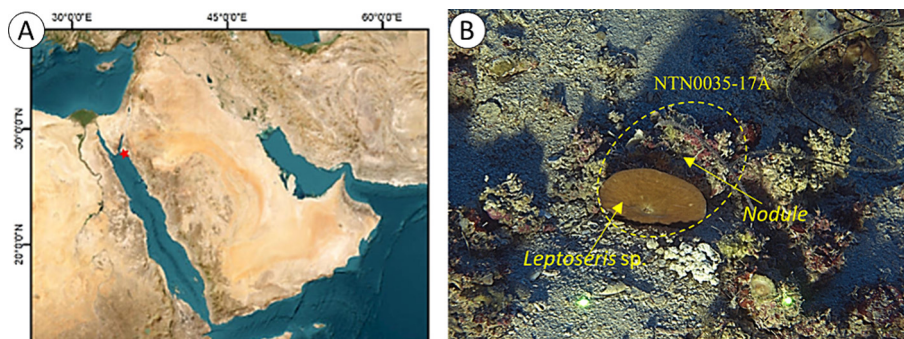

Fig. 1. (A) Map of the sampling site; (B) Sample NTN0035-17A on the seafloor at a depth of 102.8 m before the sampling.

Table 1
Summary of key μCT scan parameters.

Scan name	Voxel size (μm)	Voltage (KV)	Current (ma)	Exposure time (ms)	Averaging	Hardware filter
Low resolution- Full volume (FV)	70	90	778	28	10	1 mm Al filter
High resolution- Sub-volume (SV)	30	120	250	150	10	none

typically consists of three main steps: 1) the target classes are defined, 2) examples of each class in the input images are provided, e.g., via brushstrokes, and 3) the Random Forest classifier assigns the probabilities of each pixel belonging to each of the classes. Typically, the steps 1 and 2 are performed iteratively until satisfactory results are achieved.

We evaluated three cases of segmentation to obtain the labels based on the multi-scale image analysis and interpretations of the FAN sample. In the first case, we used only TSC for segmenting all the labels, using Ilastik image segmentation toolkit (https://www. ilastik.org/). The second segmentation case included watershed segmentation to supplement TSC. The third segmentation case included a combination of TSC and thresholding of CT intensity values. In this case, following TSC, the EF and CCA volumes were separated by first segmenting the volume corresponding to the CCA layers using greyscale thresholding, which was then mathematically subtracted from the 'EF + CCA' volume. Similarly, greyscale segmentation and subtraction operation was also performed for the void volume. The segmentation case that resulted in the most optimal results for HRCT was then applied to the full sample μCT image.

2.4.2. Full sample μCT image segmentation and analysis

Prior to segmentation, we cropped out the additional materials attached to the sample, such as the *Leptoseris* sp. corals from the LRCT, using an ellipsoid mask. Additionally, we separated the voids from the background in the LRCT image. Since they have similar range of low CT values, it is difficult to differentiate voids from background using thresholding alone. To segment the voids, we first created a binary mask of the data where background and void voxels were set to 0 and the rest to 1. We then computed the ambient occlusion for the volume to determine regions inside the binary mask which we then assigned to voids. Ambient occlusion shoots several outward rays (100 in our case) starting at each 0 voxel and counts how many 1 voxels are hit. For 0 voxels inside the binary mask, the hits will be much more than those on the outside. In this study, we assigned voids to 0 voxels that have more than 90 % hits.

To be able to take advantage of the HRCT image and corresponding segmentation results to guide the full volume LRCT segmentation, the HRCT segmented label volumes were spatially aligned with the LRCT image. This alignment of the two μCT images was done in Avizo™ by first resampling the LRCT image data (70 μm voxel size) using Lanczos filter and down sampling the HRCT scan (30 μm voxel size), resulting in both images having 60 μm voxel size. We then performed image registration using normalized mutual information as similarity metric (Studholme et al., 1999). Similarly, using the same alignment transform we spatially registered the down sampled HRCT ground truth segmentation results with LRCT. We used this aligned pair to determine the thresholding and constrain the TSC results of the LRCT data. The volume fractions of the various skeletal and sediment components of the FAN sample were obtained from the final segmented volumes of LRCT.

3. Results and discussion

## 3.1. Multi-scale characteristics of foraminiferal-algal nodule

The nodule NTN0035-17A is of sub-spheroidal shape and has the dimensions 10.3 × 7.2 × 5.6 cm (Fig. 2A). The surface of the

sample is very complex, and more than a half of the surface was buried in the sediment at the time of collection (Fig. 1B). Consequently, the sample is only partially covered by living organisms, as evidenced by the presence of *Leptoseris* sp. (Fig. 2A) (Vimercati et al., 2024), encrusting foraminifers (EF), Crustose Coralline Algae (CCA) and tubeworms. Volume and surface rendering of the full-volume LRCT image corroborated the highly irregular surface morphology and enabled the visualization of serpulid tubes and the growth of young corals on the surface of the nodule (Fig. 2B).

LRCT cross-section views revealed the distribution and morphology of the internal components of the entire nodule, corroborated by the sub-volume HRCT image that provided enhanced contrast and detail of these structures (Fig. 3A–B). We were also able to observe the potential nuclei within the nodule using the LRCT cross-sections. The greyscale values of the voxels in the CT images representing the volumes of the various components specifically correspond to their density. The darker and lighter areas on the greyscale CT image hence correspond to lower and higher density, respectively. The CT images reveal that the nodule is comprised of concentric alternating layers of high and low density, moderately continuous and interrupted by large irregularly shaped voids that often contained unstructured infill material with low density. Based on the results from the previous study of this nodule by Bracchi et al. (2023), such infill material is comprised of poorly lithified sediment. The nodule contains such a sediment-filled cavity close to the center with the longest axis measuring approximately 2 cm, and a similarly large cavity approximately 1 cm from the surface (Fig. 3A, F). Large macro-borers such as bivalves are also clearly visible, suggesting 'destructional' (*sensu* Nitsch et al., 2015) voids (Fig. 3A–B, F). Variably sized voids present along the surface of the sample indicate encrustation by biomineralization, forming 'constructional' voids (Fig. 3A, D, F).

3.1.1. Microtextural and mineralogical characteristics

Thorough visual inspection of the high and low-resolution CT images guided the selection of locations in the nodule for prepara-
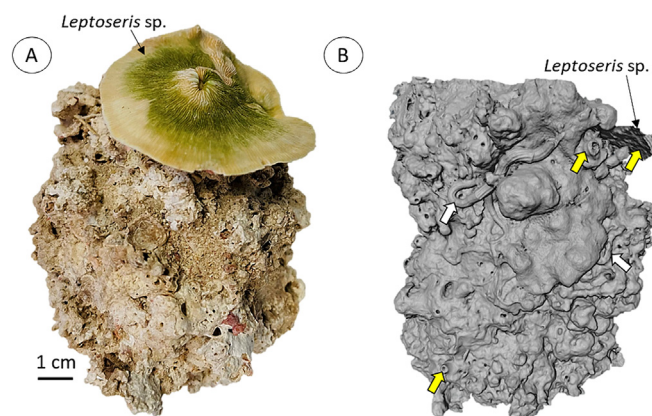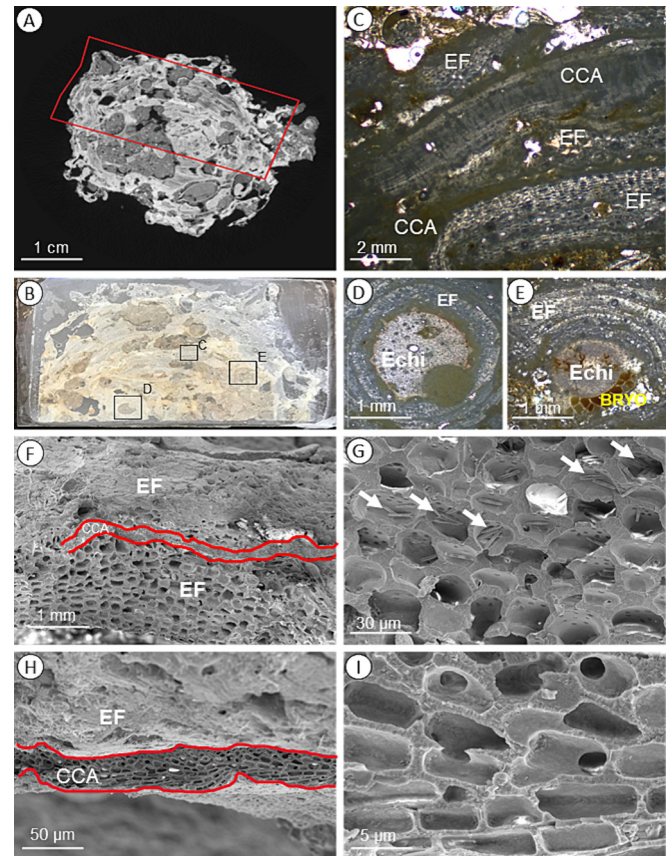

Fig. 2. (A) Sample NTN0035-17A after drying. (B) Volume rendering of the full volume x-ray CT image showing the side-view of the FAN sample NTN0035-17A, showing highly irregular surface morphology, serpulid tubes (white arrows) and young corals (yellow arrows) visible on the surface. (For interpretation of the references to colour in this figure legend, the reader is referred to the web version of this article.)
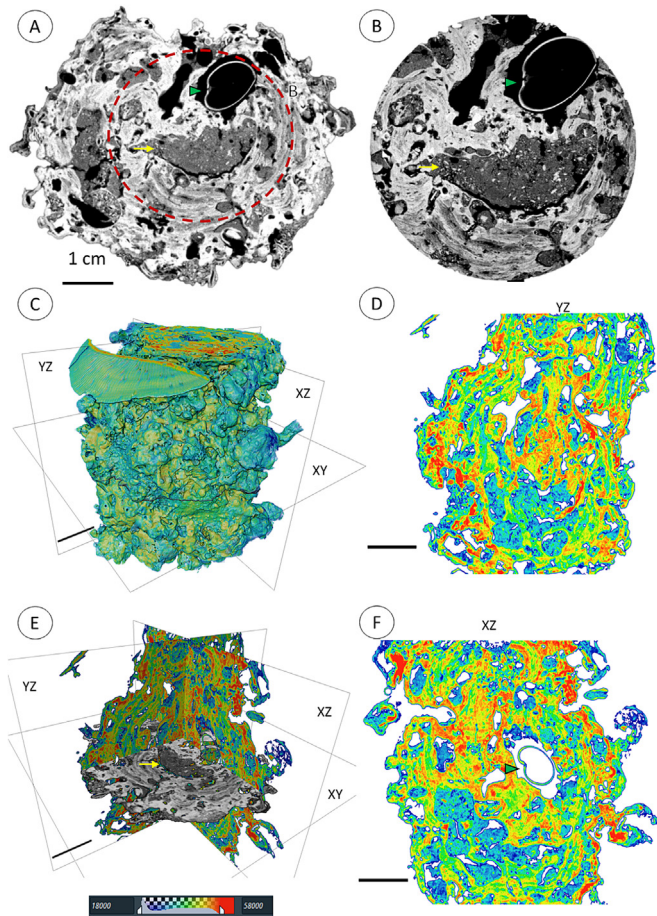
Fig. 3. Exemplary *XY*-cross sections of (A) low-resolution full volume and (B) high-resolution sub-volume scans of the nodule. The dashed circle represents the location of the sub-volume scan within the sample. Note the enhanced contrast and detail of the internal layers in the high-resolution sub-volume scan. The yellow arrows and green triangle indicate large sediment-filled cavities and a bivalve in a large void, respectively. (C-F) Exemplary YZ and XZ cross-section views of the full volume x-ray CT image of the nodule. Scale bar is 1 cm. (For interpretation of the references to colour in this figure legend, the reader is referred to the web version of this article.)


Fig. 4. The inner structure of sample NTN0035-17 visualized through CT-scan imagery, thin section and SEM. (A) x-ray CT cross-section corresponding to the thin section in B. (B) Thin section of sample NTN0035-17 with the indication of boxes magnified in C, D and E. (C) Magnification of evident layering pattern inside the structure of the nodule. EF is for Encrusting Foraminifers: layers of EF show large chambers, they are generally thick and more abundant. CCA is for Crustose Coralline Algae: layers of CCA are more dense, generally thin and less abundant. (D) Magnification of the spine of a cidaroids (ECHI is for echinoids). (E) Magnification of the spine of an echinoids, with a layer of bryozoans (BRYO) and several layers of EF. (F) Exemplary SEM images with the evidence of layering pattern made of EF and CCA. EF chambers are bigger and more easily distinguishable than CCA cells. (G) A magnification of EF chambers, with diatoms inside. (H) A detail of a CCA layer. (I) A magnification of a CCA layer with cells having a near-rectangular to D-end shape.

tion of subsamples, to conduct further investigation of the main features of interest in the nodule using optical and electron microscopy analyses (Fig. 4). The thin-section micrographs obtained using this approach were matched with the corresponding x-ray CT cross-section images (Fig. 4A-E). Thin section and SEM image analysis revealed that the inner structures of the nodule are comprised of alternating layers of thick encrusting foraminifera (EF, *Acervulina* cf. *inhaerens*) and thin Crustose Coralline Algae (CCA), distributed in an irregular, sometimes concentric, layering pattern (Fig. 4). The EF layers are made of thick crusts that envelop different other organisms like echinoids, or bryozoans fragments (Fig. 4C–E). SEM analysis of broken samples suggests that the constructional voids of the EF chambers and the CCA cells have different sizes, which is manifested by the layering patterns of the internal structure (Fig. 4F–I). The EF and CCA are easily distinguishable by their width: height ratio, which is 1.2 in EF and approximately 2 in CCA. The EF layer thickness ranges between 86 and 755 μm, with a mean value of 356.9 ± 171.3 μm, while the CCA layer thickness ranges between 29 and 329 μm, with a mean value of 115.2 ± 56.9 μm. The diameter of the EF chambers ranges between 69 and 123 μm, with a mean value of 91.9 ± 29.5 μm;

chambers height ranges between 24 and 59 μm, with a mean value of 39.4 ± 9.3 μm. EF chambers often contained rod-shaped diatoms (Fig. 4G). CCA form thinner crusts with near-rectangular to D-end shaped cells (Fig. 4C, F, H). The CCA cell diameter ranges between 3.9 and 9.6 μm, with a mean value of 3.4 ± 1.4 μm, whereas the cell height ranges between 7.1 and 17.9 μm, with a mean value of 7.3 ± 2.9 μm. The above estimations of the EF (356.9 ± 171.3 μm) and CCA (115.2 ± 56.9 μm) layer thickness obtained using optical and electron microscopy served as the reference to assess how effectively the voxel size of the μCT images represented them in 3D.

SEM analysis of polished thin-sections indicates that the EF layers are generally associated with higher porosity compared to the CCA layers, because EF chambers are generally larger than CCA cells, and due to their mineral microtextures (Fig. 5A–D). SEM-EDX point analyses suggests that the EF layer is mainly composed of HMC along with minor quantities of Si (Fig. 5A–B, Supplementary Data Fig. S1–S2). The major composition of CCA layers is also HMC, with densely packed acicular/laminar shaped crystals growing radially inward from the cell wall within the CCA cells (Fig. 5C–D, Supplementary Data Fig. S3). The EF layers are characterized by
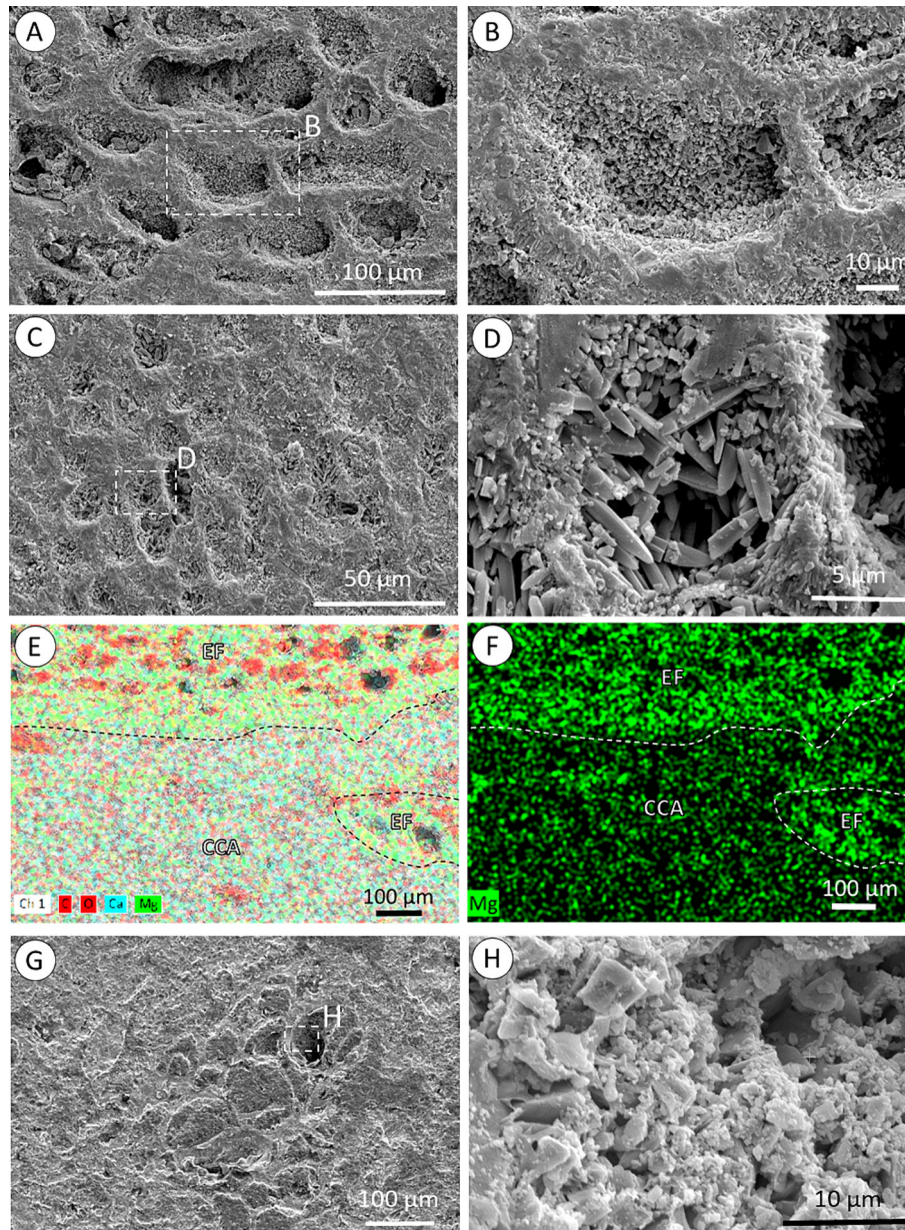
Fig. 5. Exemplary scanning electron microscopy images of polished thin sections showing the microtextures of the EF (A-B) and CCA (C-D) layers. The elemental maps resulting from Energy Dispersive X-ray (EDX) analysis show higher levels of Mg in the EF layer compared to the CCA (E-F). Micritic microtextures of the sediment infill composed of biogenic and sedimentary fragments (G-H).

higher Mg levels compared to the CCA layers, which is clearly visible in the SEM-EDX elemental map analysis (Fig. 5E–F). The infill material present in the voids of the nodule is micritic sediment composed of fine sandy and muddy, nearly lithified, biogenic and lithic fragments (Fig. 5G–H). This material occupies the cavities of the nodules that are mainly produced by boring activities, and only partially the intermittent spaces between the layers. The mineral composition of the sediment infill is high-Mg calcite, along with minor amounts of Si (Supplementary Data Fig. S4).

3.1.2. Overview and classification of inner components

As mentioned earlier, the thickness of the CCA (115.2 ± 56.9 μm) and EF (356.9 ± 171.3 μm) layers are larger than the voxel size of the high- resolution μCT scan (30 μm), suggesting the suitability of this μCT scan to represent these features in 3D. Although the visual analysis of μCT data enabled the identification of the layered

nature of the sample interior, the confirmation of the components and the micro-scale features within these layers was accurately done using the thin-section petrography and SEM analysis at higher resolutions. The integrated interpretation of μCT, thin-section and SEM analyses reveal that the inner structures of the macroid are primarily biogenic, and are predominantly made of thick EF layers and thinner layers of CCA. Based on this, the macroid can therefore be classified as a foraminiferal-algal nodule *sensu* Bosellini and Ginsburg (1971) and in agreement with Bracchi et al. (2023). As evident from LRCT cross-sections, the nodule did not develop around one single nucleus, but instead, more than one coarse biogenic fragment seem to have acted as nuclei around which layers of EF and CCA enveloped over time. Two main types of voids are present in the nodule; (i) constructional and (ii) destructional voids. The pore space in the constructional voids in this nodule is a result of the biomineralization and growth patterns

of the EF and CCA layers as well as the serpulid tubes, whereas the destructional voids were caused by boring organisms such as bivalves. The main pore types observed in the nodule according to Lucia's (1995) classification are; intergranular porosity within the sediment infill, intercrystalline porosity within the EF and CCA layers, connected vugs that include the destructional voids and isolated vugs mainly comprising the constructional voids. As discussed previously, these constructional voids are the result of CCA encrustation by biomineralization.

Four main components have been classified for quantitative μCT analysis based on the interpretations from μCT and petrography results (Fig. 6); (i) EF layers (ii) CCA layers, (iii) sediment infill, and (iv) voids. The CT intensity recorded for each of these components is directly related to their respective pore space characteristics and mineral microtextures. The CCA layers, which are characterized by densely packed HMC crystals are associated with the highest CT attenuation, and correspondingly high range of pixel values (yellow orange areas in Fig. 6), while the voids correspond to the lowest pixel value range (white areas with the sample in Fig. 6). The sediment infill and the EF layers resulted in intermediate pixel range, with an overlap of CT values between the two (Blue-green areas in Fig. 6). This similarity in x-ray CT attenuation is due to the bulk CT values resulting from the combination of total porosity and similar mineral compositions in the EF and sediment volumes. However, the micro- and macro-textures of these two components are visibly different, as apparent from the SEM images (Fig. 5). In the μCT image, the sediment infill appears as a porous and unstructured mass, in contrast to the concentric patterns formed by the EF and CCA layers (Fig. 6).

3.2. Optimal segmentation of sub-volume μCT image

The image processing steps performed as a prerequisite of μCT image segmentation, including histogram equalization and NLM filter, improved the contrast between the voxels while preserving the morphological features. This improvement in image quality is demonstrated by the CT value histograms (Supplementary Data Fig. S5). Histogram equalization spread the dynamic range of the CT pixel values, thereby making the grey-scale histogram uniform and improving the contrast between the image details. The NLM

Fig. 6. Interpretation of the inner components of the FAN sample based on multiscale-multimodal characterization using X-ray CT, optical and electron microscopy.

filter denoised the CT images while preserving important features such as edges and textures. The thresholding segmentation method we applied to the HRCT image generally works well for datasets where the components have very distinct densities resulting in clear separation of grey values. This is typically evident in peaks and valleys in the intensity value histogram of the CT images, which can be used to guide the identification of gray-value ranges for each class. In the FAN sample, the voids and the CCA have the lowest and highest CT densities, respectively, and hence their corresponding unique greyscale ranges (Fig. 6). Voids, due to their very low density, result in correspondingly low CT intensity values close to 0, and are thus relatively easy to classify via interactive thresholding guided by the histogram. Similarly, CCA, due to their very high density compared to other components, resulted in the highest CT intensity range, and were segmented via visualization-guided interactive thresholding to separate the CCA from EF layers. However, the overlap in the CT values of the CCA EF layers with the sediment infill posed a challenge to mathematically implement the visually perceived interpretations in the image segmentation process using thresholding alone. TSC method, which is a machine-learning approach that leverages on the textural image features, effectively addressed this issue. As discussed previously, although the CT values of the voxels representing the EF and sediment infill are overlapping, the CT textures manifested by their spatial distribution are visually distinguishable. However, when only TSC was used to segment all the four classes, the voids and sediment infill classes were distinguished clearly, while the EF and CCA layers could not be separated, causing gaps in the segmented images. This is due to the similarity in the textures of the EF and CCA layers, in contrast to the unique and well defined CT textural properties of the sediment infill and voids. To compensate for these gaps in the EF and CCA layers we then applied watershed algorithm. The combination of TSC and watershed methods also resulted in unsatisfactory segmentation, especially in separating the EF and CCA layers from each other. Leveraging on the insights gained from these approaches, we then used a combination of TSC and thresholding that best matched the characteristics of each of the four classes. We reformulated the TSC approach by strategically grouping the target classes into three labels corresponding to the most distinctive textural features (Fig. 7); (i) voids, (ii) sediments, and (iii) EF and CCA layers.

The iterative pixel classification pipeline of TSC method enabled us to manually label exemplary areas corresponding to each component to be segmented (Fig. 7A), and automatically label the pixels in the remaining image area using a Random Forest classifier. Correspondingly, three segmented volumes- voids, sediments and 'EF + CCA'- were obtained (Fig. 7B). This specific combination of labels proved most effective to apply the TSC approach successfully, owing to the distinctly layered CT textures of the EF-CCA layers compared to the porous and unstructured sediment volumes. Moreover, TSC segmentation effectively distinguished the CCA and EF layers from sediment infill despite the presence of bioclastic debris with CT values similar to those of CCA. As evident from the integrated μCT and SEM image analysis, the mineralogical and microtextural characteristics and their impact on skeletal density also contributed to the unique CT textures that favored TSC. Including the voids as one of the classes improved the network training and segmentation of the three simplified classes.

Finally, successful segmentation of all the four classes was achieved after integrating the CCA and void volumes- segmented using greyscale thresholding- with the TSC segmentation results (Fig. 8). The combination of thresholding and machine-learning based TSC methods subsequently resulted in the most accurate segmentation of the four classes in the FAN sample in classifying the voxels representing the voids, sediment infill, EF and CCA (Fig. 9). This hybrid segmentation approach allowed us to take
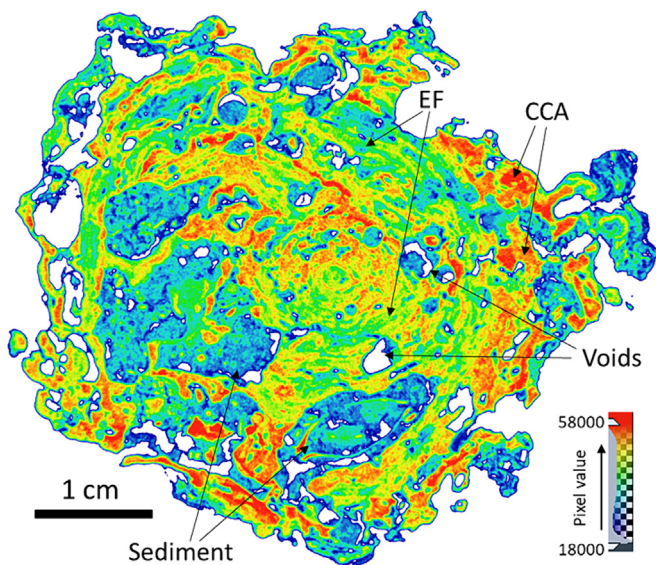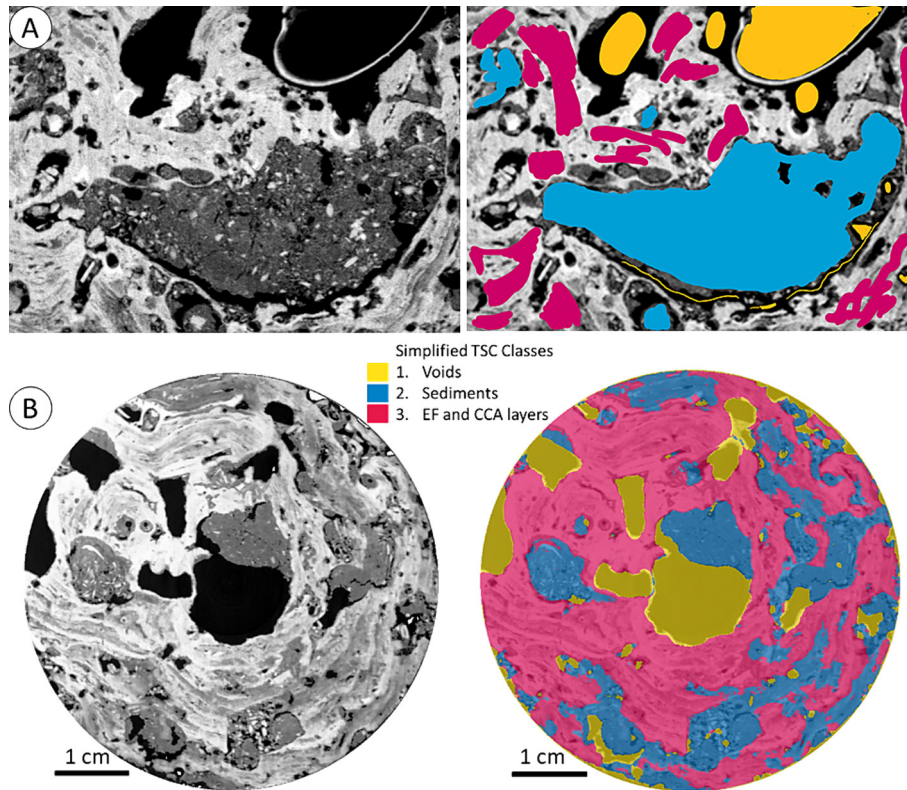
Fig. 7. (A) Demonstration of the manual labeling of the grey-scale image (left) using three simplified TSC classes (right) using ilastik to be used for training the Random Forest model for textures-based segmentation. (B) Exemplary greyscale cross-section from HRCT (left) and corresponding labelled image after applying the TSC segmentation method for the three simplified classes, overlying the greyscale image (right). Note that the areas of Sediment and EF + CCA are clearly distinguised despite the similarity of grey-scale values. Scale bar is 500 μm.

advantage of the variations in both gray-scale value ranges (voids vs CCA) and the textural distributions of the CT values (Sediment vs EF and CCA) of each class. Moreover, the manual effort required to label each class was significantly reduced compared to the other tested methods, due to the iterative pixel classification pipeline of TSC. The segmentation methodology and results thus obtained are therefore used as the 'ground-truth', to be applied for full volume LRCT segmentation.

3.3. Quantification of carbonate volumes using μCT analysis

The full volume LRCT image proved to be a valuable source of qualitative information such as the potential locations of the nuclei and the nature of the internal layers and semi-quantitative infor-

mation pertaining to the presence and distribution of the various components within the FAN sample. However, the larger voxel size in the LRCT caused increased partial volume effect compared to HRCT and higher ambiguity in the identification and segmentation of the four main components. In other words, it was challenging to determine the grey-scale thresholds or manually label the various classes during TSC using LRCT alone, especially in boundaries where the greyscale values were compromised by the higher voxel size. However, the HRCT image and ground-truth segmentation of the sub-volume offer significantly improved detail of the boundaries between the classes, especially in distinguishing the EF and CCA layers. Hence, we used the HRCT image and segmentation results to guide the segmentation of LRCT and obtain reliable quantification of the various carbonate components present in the nod-
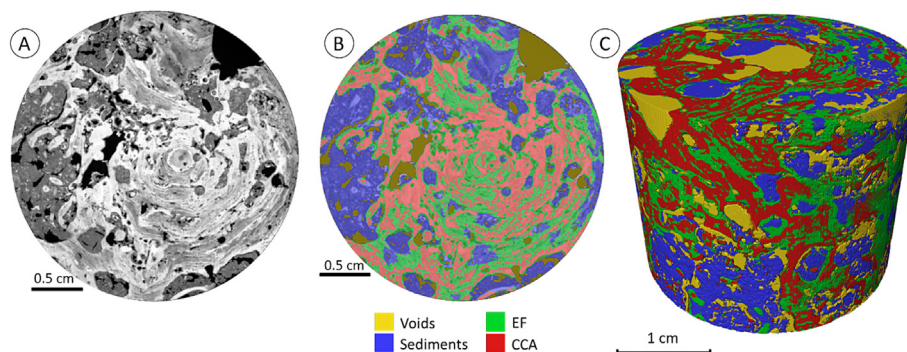

Fig. 8. Exemplary HRCT greyscale cross-section (A) and its corresponding labelled image (B) segmented into voids, sediments, EF and CCA. (C) 3D volume renderings of segmented volumes of voids, sediments, EF and CCA from the ground-truth segmentation method applied to the sub-volume HRCT image of the FAN.

Voids
Sediments
EF
CCA

1 cm
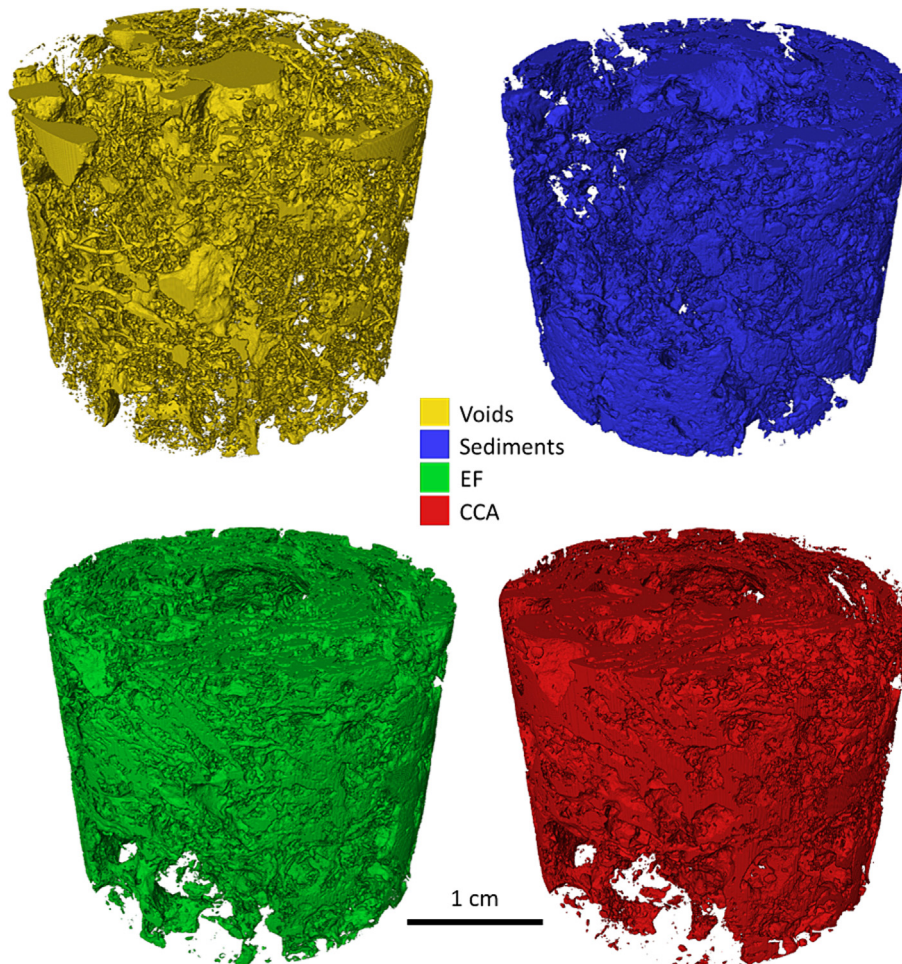
Fig. 9. 3D volume renderings of individual segmented volumes of voids, sediments, EF and CCA from the ground-truth segmentation method applied to the sub-volume HRCT image of the FAN.

ule. Resampling the HRCT and LRCT images into 60 µm voxel size led to 1-to-1 voxel mapping between them, thereby allowing us to spatially align the two images (Fig. 10). This image registration then made it possible to directly correlate the segmented HRCT image with the corresponding grey-scale LRCT image when performing hybrid segmentation using thresholding and TSC.

Cropping out the *Leptoseris sp.* coral prior to segmentation minimized the computational effort and time, and also improved the Random Forest network training during the application of TSC method. Moreover, this allowed us to separate the coral volumes from that of the nodule during quantification. Background removal using ambient occlusion computations effectively separated the voids from the voxels in the sample exterior with the same grey-scale values (Supplementary Data Fig. S6). The ground-truth segmentation labels served as the direct reference to label the simplified classes within the corresponding sub-volume in the LRCT image (Fig. 11A–B), thereby mitigating the identification and labeling challenges that arose from partial volume effect. The Random-Forest network, now armed with a larger set of training data guided by the sub-volume, effectively segmented the volumes of Voids, Sediments and "EF + CCA" from the full volume LRCT image. The Void and CCA label volumes from the ground-truth segmentation results provided the reference to determine the pixel values to be used for segmenting these classes in the LRCT image using thresholding (Fig. 11C–D). Finally, applying the same arithmetic operations as in the HRCT ground-truth methodology


1 cm   0 ▬▬▬▬▬▬ 65535
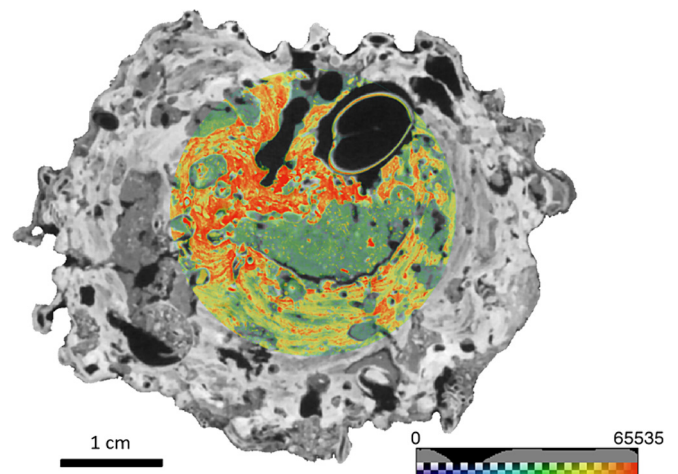
Fig.10. Exemplary cross-section of the full volume LRCT image (grey-scale) spatially registered with the HRCT image (colored area), after resampling into 60 µm.

resulted in effective segmentation of all the four main components of the nodule (Fig. 12); Voids, Sediment, EF and CCA.

The ground-truth segmentation methodology and corresponding results thus guided and constrained the segmentation of the
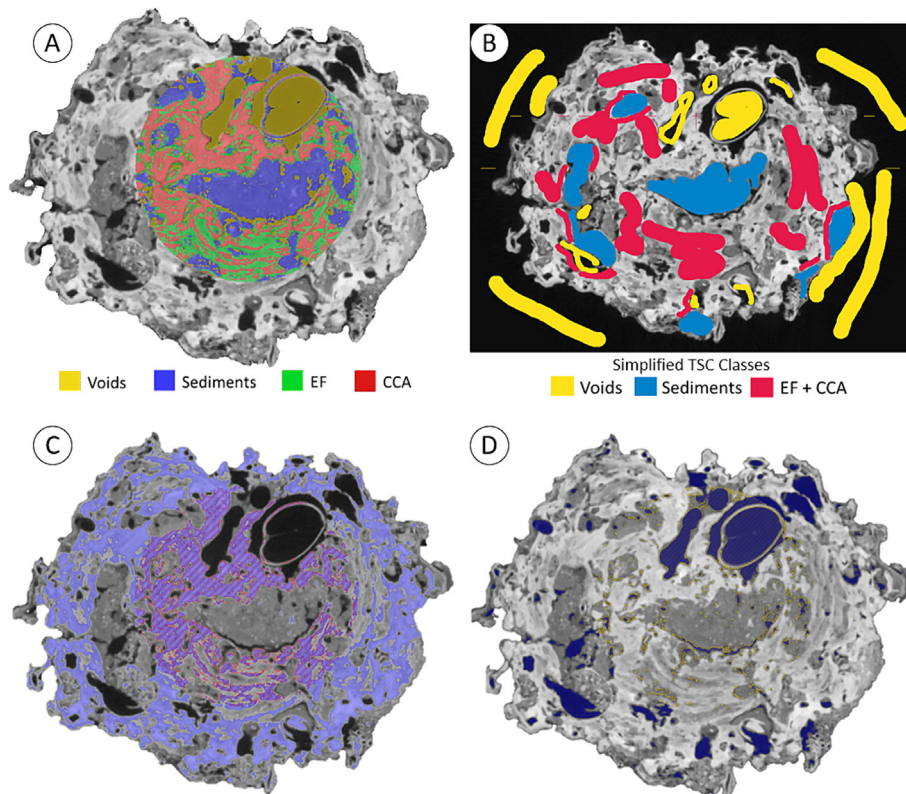
Fig. 11. (A) Exemplary cross-section of the full volume LRCT image (grey-scale) overlaid by the ground-truth segmentation results of HRCT (colored area). (B) Manual labeling of simplified TSC classes on the full volume LRCT image in ilastik guided by ground-truth, for texture-based segmentation. (C) Guided thresholding of CCA layers in full volume (blue) using the segmented CCA in HRCT (purple) as a reference. (D) Guided thresholding of voids in full volume (Blue-white) based on the segmented voids in HRCT (yellow). (For interpretation of the references to colour in this figure legend, the reader is referred to the web version of this article.)

full volume LRCT, thereby providing higher confidence in the computed volume fractions of the skeletal, void and sediment components of the FAN sample (Fig. 13) (Table 2). According to the

Fig. 12. Exemplary full volume LRCT greyscale cross-section (top left), its corresponding labelled image (top right) and full 3D volume rendering (bottom) of segmented voids, sediments, EF and CCA. Scale bar is 1 cm.

computed volume percentages of Voids, Sediments, EF and CCA within the FAN sample, approximately 65.5 % of the FAN sample is composed of the EF and CCA layers, and contributes to biogenic carbonate production (Table 2). The total volume of the sample based on previously estimated by Bracchi et al. (2023) using traditional methods is 173.3 cm^3. In the present study, the volumetric contributions obtained from the μCT analysis of the main carbonate components of the nodule were computed to be 53.72 cm^3, 69.01 cm^3 and 73.32 cm^3, corresponding to the Sediments, EF and CCA, respectively. The habitat suitability model informs us that FANs cover at least 6.72 km2 of the NEOM shelf. If nodules are spread over a net area of 287 m^2 then their average volume corresponds to 173.3 cm^3, as estimated by Bracchi et al. (2023). If we assume similar rates of carbonate production as the studied nodule, this means that 334233.312 m^3 of biogenic carbonate made by the FANs is presently at seafloor, of which 106152.499 made by EF and 112770.319 made by CCA. However, it must be noted these estimates are only indicative of the potential of carbonate production by these contributors, while in nature the nodules would indeed have variable distributions of EF and CCF carbonates. Our ongoing work includes careful selection of a larger number of representative samples to perform non-destructive μCT scanning, and application deep-learning to further improve the proposed machine-learning aided segmentation method. Moreover, the estimate of net carbonate volume needs further improvement by deducting the inter-particle and intra-particle porosity from the CCA and EF volumes.

Given the higher volumetric contribution and CT density values of CCA compared to the EF layers and sediment infill, the CCA layers are indeed associated with highest amount of carbonate production within this FAN sample. The current knowledge on how much biogenic carbonate is produced at the seafloor by less
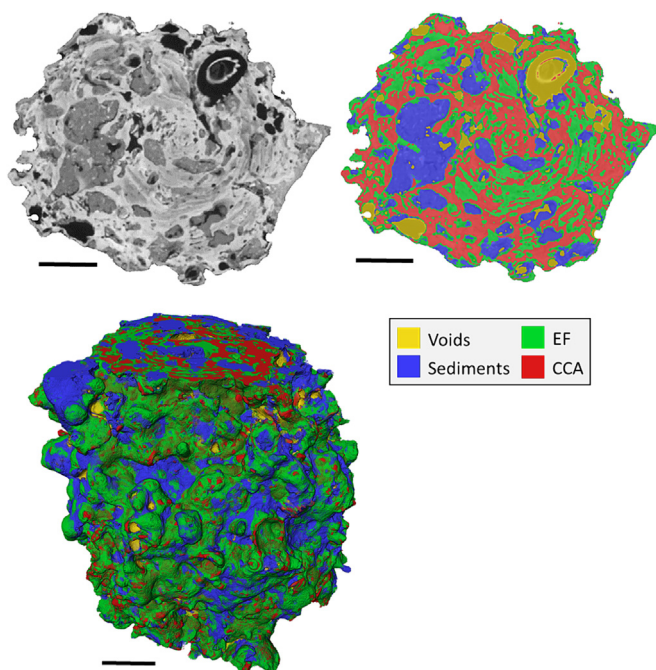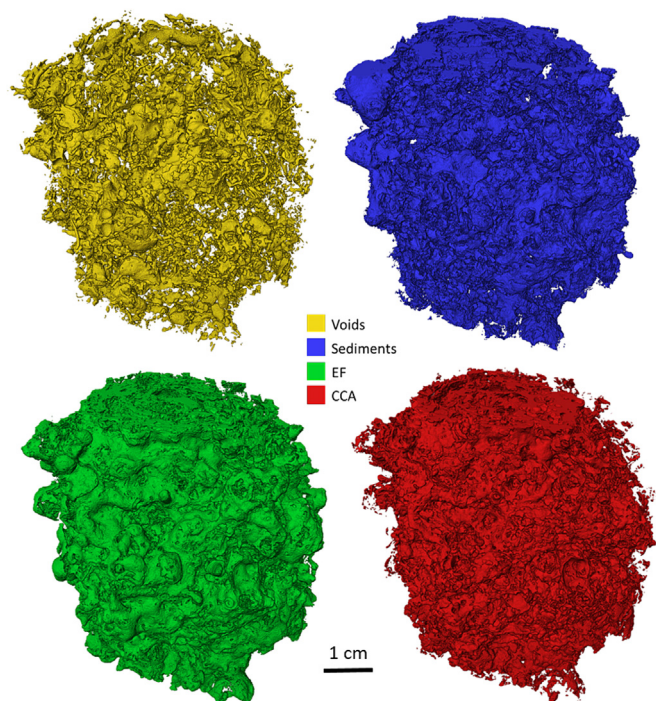
Fig. 13. Individual 3D volume renderings of Voids, Sediments, EF and CCA segmented from the LRCT image of the nodule obtained using the hybrid-segmentation method guided by the ground-truth results from HRCT image.

Table 2
Quantitative volume fraction analysis of the nodule.

Material	Voxel count	Volume (%)	Volume (cm^3)
Voids	35,348,722	9.78	21.25
Sediments	89,378,320	24.72	53.72
EF	114,845,652	31.76	69.01
CCA	121,975,705	33.74	73.32

famous builders such as encrusting foraminifers is limited and is seldom quantified and integrated in the models of carbonate production and inorganic carbon burial cycle. In this context, the results of this study provide new evidence to the substantial contribution of EF to the Red Sea carbonate budget and underscore the need for further investigation. For example, when supplemented with the exact skeletal density values of the EF and CCA layers, which is typically species dependent (Adey et al., 2013; Chan et al., 2017), their specific contributions to carbonate production can be more accurately quantified. However, estimating individual skeletal densities and their seasonal variations in these FAN samples is out of scope of this study and will be addressed in our future work. Finally, the multiscale characterization methodology proposed in this study, when assisted by deep-learning, can be applied to more samples from this FAN habitat, and will shed light on the specific inputs of these EF and CCA species to the Red Sea carbonate budget at the larger scale.

3.4. Multi-scale μCT analysis protocol and possible applications

Based on the results of this study, we propose a multiscale and multimodal approach employing μCT imaging and electron microscopy to analyze and quantify the internal components of biogenic nodules. The methodology is comprised of three main phases, Phases I- III (Fig. 14). Phase I begins with an overview μCT scan (LRCT) to capture the 3D image of the full volume of the sample,

as well as a sub-volume μCT scan with the highest possible resolution image (HRCT) in a non-destructive manner. Guided by the visualization of the inner layers using the LRCT, the sample is then cut into sub-sections to prepare petrographic thin-sections and broken segments from specific locations on which optical and electron microscopy analyses are performed. The results from the integrated analyses are then used to interpret the key components of the internal layers of the sample, each of which typically result in specific range and distributions of CT intensity values and grey-scale textures in the x-ray images, corresponding to the x-ray attenuation. The main components thus identified serve as the 'classes' to be segmented and quantified using the μCT data. In Phase II the HRCT scan is segmented into these classes using the hybrid- thresholding and texture-based-segmentation workflow, which serves as the 'ground-truth' of the segmented volumes. In Phase III the ground-truth segmented volumes are spatially registered with the LRCT scan, in order to guide the hybrid segmentation of the main classes for the entire sample volume. Finally, the segmentation results from the LRCT image are used for quantitative volumetric analysis of the full sample volume.

As discussed previously, a broad range of biophysical and chemical factors in conjunction with erosion processes (Scoffin, 1993; Perry et al., 2012, Montaggioni and Braithwaite, 2009) controls biogenic carbonate production, namely the amount of biogenic carbonate that accumulates through time. The rates at which production and erosion operate strongly influence net carbonate production rates (=carbonate budget). Standardized census-based methodologies present the opportunity to reliably estimate carbonate budgets and allow comparison over time or across local and regional scales. Our study provides a systematic protocol to identify and analyze the various builders, even the less well-studied biogenic carbonate producers such as encrusting foraminifera, and to quantify taxa-specific gross carbonate production. The multi-scale μCT analysis methodology we developed in this study − the combination of high resolution sub-volume and lower resolution full volume images- is suitable for 3D characterization of a wide range of calcareous marine skeletal structures. This is a non-destructive and easily replicable approach to obtain taxa-specific quantification, which would otherwise require substantial efforts and time for sampling and analysis.

Furthermore, marine biogenic carbonate structures are being increasingly used as paleo-environmental proxies to improve the understanding of the oceans' response to rising atmospheric CO_2 levels, and corresponding impact on marine biogeochemical cycles and carbonate production (Andersson et al., 2008; Halfar et al., 2013; Enochs et al., 2016a; Byrne and Fitzer, 2019; Kawahata et al., 2019). As such, our proposed methodology (Fig. 14) is readily applicable to study such biogenic structures for the quantification of structural characteristics such as voids and calcified components. The hybrid segmentation methodology we adopted in this study (Phase II and III in Fig. 14) is expected to be particularly useful for the analysis of biogenic structures in which the inner textures and components are distinctly visible despite having an overlap in the range of CT intensity values. When combined with additional geochemical data, such as radiocarbon dating, the volumetric analysis results from the proposed methodology can be used to quantify the growth rates of calcareous marine structures with banded patterns such as corals, rhodoliths, foraminiferal-algal nodules, banded CCA build-ups, and so on, in which the alternations of high and low density bands reflect the seasonal and environmental changes. Other possible applications include the quantification of macro-bioerosion associated with changes in carbonate skeletal integrity in response to ocean acidification, and related effects on net carbonate production rates (Wisshak et al., 2012; Crook et al., 2013; Enochs et al., 2016b). Quantitative methods such as the one presented in this study thus offer a reliable
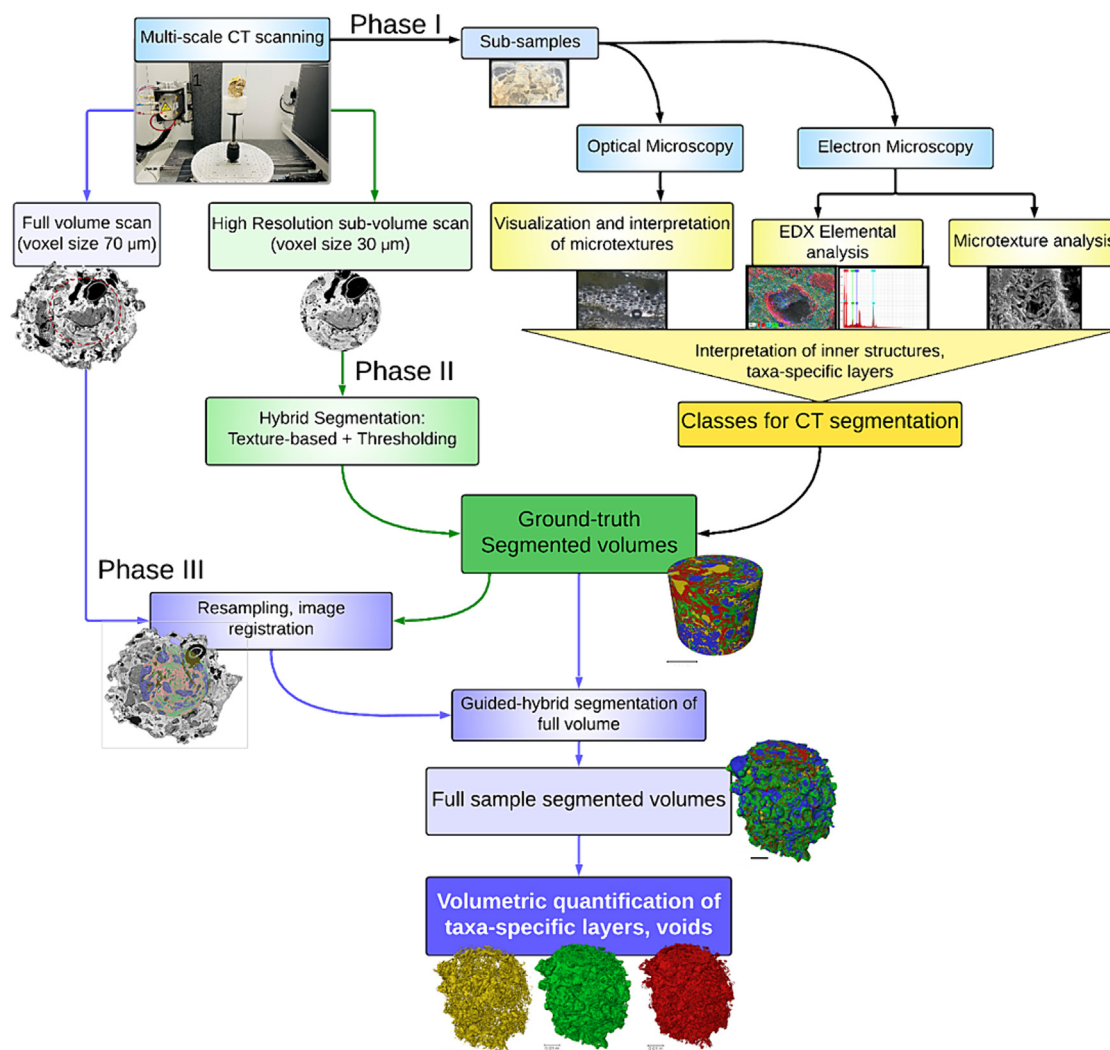
Fig. 14. Schematic of multi-scale multi-modal analysis methodology employed in this study to characterize the Foraminiferal-Algal Nodule (FAN) sample.

account of benthic carbonates across seas, and provide the much needed information to evaluate risks and consequences of future climate change and the possible effects on marine life and ecology.

4. Conclusions

In this study, we applied a novel multi-scale μCT image analysis methodology combined with electron microscopy and image based machine learning to characterize and quantify the major carbonate components of a foraminiferal-algal nodule (FAN) from the Red Sea, Saudi Arabia. Four main components have been identified based on the integrated μCT and SEM analysis (i) encrusting foraminifers (EF) (ii) crustose Coralline Algae (CCA), (iii) Sediment infill, and (iv) Voids. The inner structures of the macroid are thus primarily biogenic, and are predominantly made of alternating thick EF layers and thinner layers of CCA, distributed in an irregular layered pattern. Two main types of voids are present in the nodule; (i) Constructional and (ii) Destructional voids. SEM-EDX analysis confirmed that the FAN is primarily composed of Ca-Mg-carbonates, with the EF layers containing higher levels of Mg compared to the CCA layers. The CT intensity recorded for each of these components is directly related to their respective pore space characteristics and mineral microtextures. The concentric arrangement

of the EF and CCA layers, attributed to their respective biomineralization and accretion mechanisms, has manifested in their distinguished signatures of CT textures.

The hybrid segmentation approach of thresholding and machine-learning based texture-supervised classification (TSC) provided an elegant solution to accurately segment the main components of the FAN, with minimal manual effort to label the classes. This approach is suitable for the analysis of wide range of biogenic structures in which the textures and components of the internal layers are distinctly visible despite having an overlap in the range of CT density values. Resampling and registering high resolution μCT segmentation results with the lower resolution full volume μCT image guided and constrained the segmentation of the latter, thereby providing higher confidence in the computed volume fractions of the skeletal, void and sediment components of the FAN. The highest biogenic carbonate production in this FAN sample is attributed to the CCA layers (33.74 %), due to the combination of their high volume fraction and CT density values, followed by EF (31.76 %). The multi-scale μCT analysis approach, supported by expert-guided interpretations based on electron microscopy imagery, thus improved the individual quantification of the carbonate components, including the thin CCA layers. Moreover, the methodology developed for this study is suitable for analyzing biogenic carbonate structures for a wide array of

applications including quantification of carbonate production and studying the impact of ocean acidification on skeletal structures of marine calcifiers.

CRediT authorship contribution statement

Declaration of competing interest

The authors declare that they have no known competing financial interests or personal relationships that could have appeared to influence the work reported in this paper.

Acknowledgements

Appendix A. Supplementary data

Supplementary data to this article can be found online at https://doi.org/10.1016/j.gsf.2024.101883.

References

Abdullah-Al-Wadud, M., Kabir, M.H., Dewan, M.A.A., Chae, O., 2007. A dynamic histogram equalization for image contrast enhancement. IEEE Trans. Consum. Elect. 53 (2), 593–600.

Adey, W., Halfar, J., Williams, B., 2013. Biological, physiological and ecological factors controlling high magnesium carbonate formation and producing a precision Arctic/Subarctic marine climate archive: The coralline genus Clathromorphum Foslie emend Adey. Smithson. Contrib. Mar. Sci. 40, 1–48.

Andersson, A.J., Mackenzie, F.T., Bates, N.R., 2008. Life on the margin: implications of ocean acidification on Mg-calcite, high latitude and cold-water marine calcifiers. Mar. Ecol. Prog. Ser. 373, 265–273.

Bassi, D., Iryu, Y., Humblet, M., Matsuda, H., Machiyama, H., Sasaki, K., Matsuda, S., Arai, K., Inoue, H., 2012. Recent macroids on the Kikai-jima shelf, Central Ryukyu Islands. Japan. Sedimentol. 59 (7), 2024–2041.

Berg, S., Kutra, D., Kroeger, T., Straehle, C.N., Kausler, B.X., Haubold, C., Schiegg, M., Ales, J., Beier, T., Rudy, M., Eren, K., 2019. Ilastik: interactive machine learning for (bio) image analysis. Nat. Methods 16 (12), 1226–1232.

Bosellini, A., Ginsburg, R.N., 1971. Form and internal structure of recent algal nodules (rhodolites) from Bermuda. J. Geol. 79 (6), 669–682.

Bosence, D.W., 1983. The occurrence and ecology of recent rhodoliths—a review. Coated Grains. Springer, Berlin Heidelberg, Berlin, pp. 225–242.

Bosence, D.W., Pedley, H.M., 1982. Sedimentology and palaeoecology of a Miocene coralline algal biostrome from the Maltese Islands. Palaeogeogr. Palaeocl. Palaeoecol. 38 (1–2), 9–43.

Bosence, D.W.J., Wilson, J., 2003. Maerl growth, carbonate production rates and accumulation rates in the northeast Atlantic. Aquatic Conservation: Marine and Freshwater Ecosystems 13, S21–S31.

Bracchi, V.A., Bazzicalupo, P., Fallati, L., Varzi, A.G., Savini, A., Negri, M.P., Rosso, A., Sanfilippo, R., Guido, A., Bertolino, M., Costa, G., 2022. The main builders of Mediterranean coralligenous: 2D and 3D quantitative approaches for its identification. Front. Earth Sci. 10, 910522.

Bracchi, V.A., Purkis, S.J., Marchese, F., Nolan, M.K., Terraneo, T.I., Vimercati, S., Chimienti, G., Rodrigue, M., Eweida, A., Benzoni, F., 2023. Mesophotic foraminiferal-algal nodules play a role in the Red Sea carbonate budget. Communicat. Earth Environ. 4 (1), 288.

Breiman, L., 2001. Random forests. Mach. Learn. 45, 5–32.

Bressan, G., Favretto, S., Kaleb, S., Tromba, G., 2007a. Applicazione della microtomografia computerizzata a raggi X allo studio predittivo della struttura di alghe rosse calcaree. Biol. Mar. Mediterr 14 (2), 146–147.

Bressan, G., Kaleb, S., Favretto, S., Tromba, G., Vita, F., 2007b. X-ray microtomography application to a predictive evaluation of coralline algae structure. Elettra Synchrotrone Research Highlights 06–07, 29–30.

Bromley, R.G., Beuck, L., Ruggiero, E.T., 2008. Endolithic sponge versus terebratulid brachiopod, Pleistocene, Italy: accidental symbiosis, bioclaustration and deformity. Current Developments in Bioerosion, 361–368.

Buades, A., Coll, B., Morel, J.M., 2005. June. A non-local algorithm for image denoising. In 2005 IEEE Comp. Soc. Confer. Comp. Vision Patt. Recog. 2, 60–65.

Byrne, M., Fitzer, S., 2019. The impact of environmental acidification on the microstructure and mechanical integrity of marine invertebrate skeletons. Conservat. Physiol. 7 (1), coz062.

Chan, P., Halfar, J., Norley, C.J.D., Pollmann, S.I., Adey, W., Holdsworth, D.W., 2017. Micro-computed tomography: Applications for high-resolution skeletal density determinations: An example using annually banded crustose coralline algae. Geochem. Geophys., Geosyst. 18 (9), 3542–3553.

Cnudde, V., Boone, M.N., 2013. High-resolution X-ray computed tomography in geosciences: A review of the current technology and applications. Earth Sci. Rev. 123, 1–17.

Cornwall, C.E., Carlot, J., Branson, O., Courtney, T.A., Harvey, B.P., Perry, C.T., Andersson, A.J., Diaz-Pulido, G., Johnson, M.D., Kennedy, E., Krieger, E.C., 2023. Crustose coralline algae can contribute more than corals to coral reef carbonate production. Communicat. Earth Environ. 4 (1), 105.

Crook, E.D., Cohen, A.L., Rebolledo-Vieyra, M., Hernandez, L., Paytan, A., 2013. Reduced calcification and lack of acclimatization by coral colonies growing in areas of persistent natural acidification. Proc. Nat. Acad. Sci. 110 (27), 11044–11049.

Dade, W.B., 1984. Holocene multilaminar bryozoan masses–The 'rolling stones' or 'ectoproctaliths' as potential fossils in barrier-related environments of coastal Virginia. Geol. Soc. Am. Abstracts with Programs 16, 132.

Depeursinge, A., Fageot, J., Al-Kadi, O.S., 2017. Fundamentals of texture processing for biomedical image analysis: A general definition and problem formulation. In: Biomedical Texture Analysis. Academic Press, pp. 1–27.

Di Geronimo, I., Di Geronimo, R., Rosso, A., Sanfilippo, R., 2002. Structural and taphonomic analysis of a columnar coralline algal build-up from SE Sicily. Geobios 35, 86–95.

Enochs, I.C., Manzello, D.P., Wirshing, H.H., Carlton, R., Serafy, J., 2016a. Micro-CT analysis of the Caribbean octocoral Eunicea flexuosa subjected to elevated p CO2. ICES J. Mar. Sci. 73 (3), 910–919.

Enochs, I.C., Manzello, D.P., Kolodziej, G., Noonan, S.H., Valentino, L., Fabricius, K.E., 2016b. Enhanced macroboring and depressed calcification drive net dissolution at high-CO2 coral reefs. Proc. Royal Soc. B: Biol. Sci. 283 (1842), 20161742.

Focke, J.W., G, C.D., 1978. Marine lithification of reef rock and rhodolites at a fore-reef slope locality (-50 m) off bermuda. Geologie En Mijnbouw 57, 163–171.

Fordyce, A.J., Knuefing, L., Ainsworth, T.D., Beeching, L., Turner, M., Leggat, W., 2020. Understanding decay in marine calcifiers: Micro-CT analysis of skeletal structures provides insight into the impacts of a changing climate in marine ecosystems. Methods Ecol. Evolution 11 (9), 1021–1041.

Foster, M.S., 2001. Rhodoliths: between rocks and soft places. J. Phycol. 37 (5), 659–667.

Gastal, E.S., Oliveira, M.M., 2012. Adaptive manifolds for real-time high-dimensional filtering. ACM Trans. Graphics 31 (4), 1–13.

Gilbert, P.U., Bergmann, K.D., Boekelheide, N., Tambutté, S., Mass, T., Marin, F., Adkins, J.F., Erez, J., Gilbert, B., Knutson, V., Cantine, M., 2022. Biomineralization: Integrating mechanism and evolutionary history. Sci. Adv. 8 (10), eabl9653.

Gill, G.A., Coates, A.G., 1977. Mobility, growth patterns and substrate in some fossil and Recent corals. Lethaia 10 (2), 119–134.

Halfar, J., Adey, W.H., Kronz, A., Hetzinger, S., Edinger, E., Fitzhugh, W.W., 2013. Arctic sea-ice decline archived by multicentury annual-resolution record from crustose coralline algal proxy. Proc. Nat. Acad. Sci. 110 (49), 19737–19741.

Heap, A.D., Harris, P.T., Fountain, L., 2009. Neritic carbonate for six submerged coral reefs from northern Australia: Implications for Holocene global carbon dioxide. Palaeogeogr. Palaeocl. Palaeoecol. 283 (1–2), 77–90.

Hill, R., Bellgrove, A., Macreadie, P.I., Petrou, K., Beardall, J., Steven, A., Ralph, P.J., 2015. Can macroalgae contribute to blue carbon? An A Ustralian Perspective. Limnol. Oceanogr. 60 (5), 1689–1706.

Hsieh, J., 2003. Computed tomography: principles, design, artifacts, and recent advances.DOI:10.1117/3.2197756.

Kawahata, H., Fujita, K., Iguchi, A., Inoue, M., Iwasaki, S., Kuroyanagi, A., Maeda, A., Manaka, T., Moriya, K., Takagi, H., Toyofuku, T., 2019. Perspective on the response of marine calcifiers to global warming and ocean acidification—Behavior of corals and foraminifera in a high CO2 world "hot house". Prog. Earth Planet. Sci. 6 (1), 1–37.

Laforsch, C., Christoph, E., Glaser, C., Naumann, M., Wild, C., Niggl, W., 2008. A precise and non-destructive method to calculate the surface area in living

scleractinian corals using X-ray computed tomography and 3D modeling. Coral Reefs 27, 811–820.

Leal, R.N., Bassi, D., Posenato, R., Amado-Filho, G.M., 2012. Tomographic analysis for bioerosion signatures in shallow-water rhodoliths from the Abrolhos Bank. Brazil. J. Coastal Res. 28 (1), 306–309.

Li, Y., Liao, X., Bi, K., Han, T., Chen, J., Lu, J., He, C., Lu, Z., 2021. Micro-CT reconstruction reveals the colony pattern regulations of four dominant reef-building corals. Ecol. Evol. 11 (22), 16266–16279.

Logan, B.W., Harding, J.L., Ahr, W.M., Williams, J.D., Snead, R.G., 1969. Late Quaternary carbonate sediments of Yucatan shelf, Mexico. Carbonate sediments and reefs, Yucatan Shelf, Mexico (Vol. 11, pp. 1-128).

Macreadie, P.I., Serrano, O., Maher, D.T., Duarte, C.M., Beardall, J., 2017. Addressing calcium carbonate cycling in blue carbon accounting.

Marcondes Machado, F., Passos, F.D., Giribet, G., 2019. The use of micro-computed tomography as a minimally invasive tool for anatomical study of bivalves (Mollusca: Bivalvia). Zoological J. Linnean Soc. 186 (1), 46–75.

Martínez-Sanjuán, J., Kocot, K., García-Álvarez, Ó., Candás, M., Díaz-Agras, G., 2022. Computed microtomography (Micro-CT) in the anatomical study and identification of Solenogastres (Mollusca). Front. Mar. Sci. 8, 2012.

Milliman, J.D., Droxler, A.W., 1995. Calcium carbonate sedimentation in the global ocean: linkages between the neritic and pelagic environments. Oceanography 8 (3), 92–94.

Minoura, K., Nakamori, T., 1982. Depositional environment of algal balls in the Ryukyu Group, Ryukyu Islands, southwestern Japan. J. Geol. 90 (5), 602–609.

Montaggioni, L.F., Braithwaite, C.J.R., 2009. Chapter five patterns of carbonate production and deposition on Reefs. Develop. Marine Geol. 5, 171–222.

Naumann, M.S., Niggl, W., Laforsch, C., et al., 2009. Coral surface area quantification–evaluation of established techniques by comparison with computer tomography. Coral Reefs 28, 109–117. https://doi.org/10.1007/s00338-008-0459-3.

Nitsch, F., Nebelsick, J.H., Bassi, D., 2015. Constructional and destructional patterns—void classification of rhodoliths from Giglio Island. Italy. Palaios 30 (9), 680–691.

Orszag-Sperber, F., Poignant, A.F., Poisson, A., 1977. Paleogeographic significance of rhodolites: some examples from the Miocene of France and Turkey. In: Fossil Algae: Recent Results and Developments. Springer, Berlin Heidelberg, Berlin, pp. 286–294.

Perry, C.T., Edinger, E.N., Kench, P.S., Murphy, G.N., Smithers, S.G., Steneck, R.S., Mumby, P.J., 2012. Estimating rates of biologically driven coral reef framework production and erosion: a new census-based carbonate budget methodology and applications to the reefs of Bonaire. Coral Reefs 31, 853–868.

Perry, C.T., Smithers, S.G., 2011. Cycles of coral reef 'turn-on', rapid growth and 'turn-off' over the past 8500 years: A context for understanding modern ecological states and trajectories. Global Change Biol. 17 (1), 76–86.

Peryt, T.M., 1983. Classification of coated grains. Coated Grains. Springer, Berlin Heidelberg, Berlin, pp. 3–6.

Prager, E.J., Ginsburg, R.N., 1989. Carbonate nodule growth on Florida's outer shelf and its implications for fossil interpretations. Palaios 4, 310–317.

Reid, R.P., MacIntyre, I.G., 1988. Foraminiferal-algal nodules from the eastern Caribbean: growth history and implications on the value of nodules as paleoenvironmental indicators. Palaios 3, 424–435.

Ridgwell, A., Zeebe, R.E., 2005. The role of the global carbonate cycle in the regulation and evolution of the Earth system. Earth Planet. Sci. Lett. 234 (3–4), 299–315.

Roche, R.C., Abel, R.A., Johnson, K.G., Perry, C.T., 2010. Quantification of porosity in Acropora pulchra (Brook 1891) using X-ray micro-computed tomography techniques. J. Exp. Mar. Biol. Ecol. 396 (1), 1–9.

Schlager, W., 2000. Sedimentation rates and growth potential of tropical, cool-water and mud-mound carbonate systems. Geol. Soc. London Special Publ. 178 (1), 217–227.

Schönberg, C.H., Shields, G., 2008. Micro-computed tomography for studies on Entobia: transparent substrate versus modern technology. Current Developments in Bioerosion, 147–164.

Schrag, D.P., Higgins, J.A., Macdonald, F.A., Johnston, D.T., 2013. Authigenic carbonate and the history of the global carbon cycle. Science 339 (6119), 540–543.

Scoffin, T.P., 1993. The geological effects of hurricanes on coral reefs and the interpretation of storm deposits. Coral reefs 12, 203–221.

Scoffin, T.P., Stoddart, D.R., Tudhope, A.W., Woodroffe, C., 1985. Rhodoliths and coralliths of Muri Lagoon, Rarotonga, Cook Islands. Coral Reefs 4, 71–80.

Spalding, M.D., Grenfell, A.M., 1997. New estimates of global and regional coral reef areas. Coral Reefs 16, 225–230.

Speijer, R., Van Loo, D., Masschaele, B., Vlassenbroeck, J., Cnudde, V., Jacobs, P., 2008. Quantifying foraminiferal growth with high-resolution X-ray computed tomography: New opportunities in foraminiferal ontogeny, phylogeny, and paleoceanographic applications. Geosphere 4 (4), 760–763. https://doi.org/10.1130/GES00176.1.

Studholme, C., Hill, D.L., Hawkes, D.J., 1999. An overlap invariant entropy measure of 3D medical image alignment. Pattern Recogn. 32 (1), 71–86.

Tapanila, L., 2008. The medium is the message: imaging a complex microboring (Pyrodendrina cupra igen. n., isp. n.) from the early Paleozoic of Anticosti Island, Canada. Current developments in Bioerosion, 123–145.

Teichert, S., 2014. Hollow rhodoliths increase Svalbard's shelf biodiversity. Sci. Reports 4 (1), 6972.

Toomy, D.F., 1975. Rhodoliths from the Upper Paleozoic of Kansas and the Recent-a comparison: Neues Jahrbuch fur Geologie und Palaontologie. Monatschefte 4, 242–255.

Torrano-Silva, B.N., Ferreira, S.G., Oliveira, M.C., 2015. Unveiling privacy: Advances in microtomography of coralline algae. Micron. 72, 34–38.

Vale, N.F., Amado-Filho, G.M., Braga, J.C., Brasileiro, P.S., Karez, C.S., Moraes, F.C., Bahia, R.G., Bastos, A.C., Moura, R.L., 2018. Structure and composition of rhodoliths from the Amazon River mouth. Brazil. J. South Am. Earth Sci. 84, 149–159.

Van Der Heijden, L.H., Kamenos, N.A., 2015. Reviews and syntheses: Calculating the global contribution of coralline algae to total carbon burial. Biogeosciences 12 (21), 6429–6441.

Vecsei, A., 2004. A new estimate of global reefal carbonate production including the fore-reefs. Global Planet. Change 43 (1–2), 1–18.

Vimercati, S., Terraneo, T.I., Castano, C.B., Barreca, F., Hume, B.C., Marchese, F. … Benzoni, F., 2024. Consistent Symbiodiniaceae community assemblage in a mesophotic-specialist coral along the Saudi Arabian Red Sea. Front. Marine Sci. 11, 1264175.

Wisshak, M., Schönberg, C.H., Form, A., Freiwald, A., 2012. Ocean acidification accelerates reef bioerosion. Plos One 7 (9), e45124.